JOURNAL OF SOLID STATE CHEMISTRY **139,** 168–175 (1998)
ARTICLE NO. SC987828

A ^{57}Fe Mössbauer Study of REBa$_2$Fe$_3$O$_{8+w}$ Triple Perovskites with Varied Oxygen Content (RE = Dy, Er, and Y)

J. Lindén

Department of Physics, Åbo Akademi, FIN-20500 Turku, Finland

A. Kjekshus and P. Karen

Department of Chemistry, University of Oslo, N-0315 Oslo, Norway

J. Miettinen

Department of Engineering Physics, Helsinki University of Technology, FIN-02013 Espoo, Finland

and

M. Karppinen

Laboratory of Inorganic and Analytical Chemistry, Helsinki University of Technology, FIN-02015 Espoo, Finland

Received October 1, 1997; in revised form March 20, 1998; accepted March 20, 1998

REBa$_2$Fe$_3$O$_{8+w}$ phases (RE = Dy, Er, and Y) with a varied oxygen content ($-0.25 < w < 0.10$ in general, widest for RE = Dy, narrowest for RE = Er) have been obtained by quenching from controlled atmospheres. The triple-perovskite-type structure is adopted for these phases, with two crystallographically different iron atoms, tetragonal above $w \approx -0.15$ and orthorhombic below that oxygen content. The valence and spin states of iron are investigated using ^{57}Fe Mössbauer spectroscopy. At room temperature, an antiferromagnetic ordering is observed for all values of w. Six- and five-coordinated Fe^{3+}, $S = \frac{5}{2}$ environments are distinguished in the Mössbauer spectra and their occupancies for $w = 0$ are in the exact structural ratio of these two coordinations. For $w > 0$, tetravalent iron ($S = 2$) accompanies the extra oxygen atoms at the (originally) square-pyramidal Fe site, whereas divalent iron ($S = 2$) accompanies the oxygen vacancies formed in the octahedral Fe site when $w < 0$. The latter splits into two components, the intensities of which correspond to the fractions of five- and four-coordinated iron with a random distribution of meridial oxygen vacancies in an octahedron.

Key Words: **Rare earth barium iron oxides; triple perovskites; Mössbauer spectroscopy; Fe valence and spin state; statistics of; antiferromagnetic order of.**

I. INTRODUCTION

The present study represents a continuation of our endeavors to explore the properties of the rare earth (RE) phases of the iron analog (REBa$_2$Fe$_3$O$_{8+w}$) of the REBa$_2$Cu$_3$O$_{6+w'}$ cuprates. The previous Mössbauer study (1), concerned with LaBa$_2$Fe$_3$O$_{8+w}$, uncovered a number of interesting features. The most important finding was the unequivocal demonstration that the crystallographically equivalent iron atoms in the disordered (simple cubic) aristotype perovskite structure of LaBa$_2$Fe$_3$O$_{8+w}$ occur in coordination environments dictated by the random distribution of oxygen vacancies and that the valence and spin states with ordered and disordered magnetic moments follow closely the Fe oxidation state obtained by chemical analysis. The principal motivation for the present study was to check how structural ordering influences the valence and spin state distributions.

The fundamental difference between these two limiting cases of the REBa$_2$Fe$_3$O$_{8+w}$ series is that the RE = La phase is of the cubic perovskite type with almost full occupancy at the oxygen sites when w approaches 1 on oxygen saturation, whereas for RE = Dy, Er, and Y it adopts a typical triple-perovskite-type ordering of RE and Ba and octahedral and square-pyramidal oxygen coordinations around iron, with w close to zero (2–4). The RE = La version with its wide span in oxygen content does not structurally order even when the oxygen content is reduced to $w = 0$, according to the powder neutron diffraction (PND) study in ref 3. Both Mössbauer investigations (1, 5) and high-resolution electron microscopy (HREM) studies (6) indicate a very limited degree of ordering within the intergrown structural

0022-4596/98 $25.00

microdomains in the RE = La variant. On the other hand, the triple-perovskite-type phases are also well ordered on the HREM resolution scale, as judged by the results (7) for RE = Dy and Ho.

In this study we are concerned with the use of Mössbauer spectroscopy to discern the coordination and spin states for the iron atoms in the triple-perovskite-type structure upon variations in oxygen content. Great care was taken to obtain high reproducibility of any occurring disorder, and this was accomplished by equilibration and rapid quenching from a constant temperature.

II. EXPERIMENTAL

Syntheses

The samples were synthesized from nanoscale precursors obtained by liquid mixing in citrate melts (8). Standardized high-purity components were used: dry, annealed Dy_2O_3, Er_2O_3, and Y_2O_3 (>99.9%, Molycorp) and dried barium carbonate (0.1% Sr, Merck). Iron lumps (99.95%, Koch–Light) were converted to nitrate by diluted HNO_3 (Baker, analyzed) prior to adding to the melted citric acid monohydrate (99%, Fluka) into which RE_2O_3 already had been dissolved (1 mol of RE_2O_3 per 48 mol of citric acid). When the evolution of nitrous gases ceased, water was added and $BaCO_3$ was dissolved. The clear viscous melt, formed by the subsequent evaporation of water, was dehydrated into a solid at 180°C and milled, and the resulting fine powder was slowly incinerated in a crucible over 2 days at 450°C in air. Thus obtained precursors were calcined at 1000°C for 16 hr in a flow of oxygen, pressed into tablets, and fired two times for 100 hr at 1100°C (RE = Dy and Y) or at 1050°C (RE = Er) in O_2, with intermediate rehomogenization. These samples served as the REBa$_2$Fe$_3$O$_{8+w}$ master samples for the oxygen content control step in the region of $w > 0$. The RE = Dy, Er, and Y master samples for $w < 0$ were obtained by reduction and sintering (to $< 5\%$ porosity) at 900°C in flowing Ar/H_2 atmospheres with Ar/H_2 ratios of (p_{H_2O} in parentheses) 25 (0.015 bar), 42 (0.019 bar), and 17 (0.018 bar), respectively. This procedure shortened the subsequent equilibration time by eliminating the slow crossing over the stoichiometric (trivalent Fe) composition as well as diminishing the reoxidation rate of divalent Fe.

Oxygen Content Control

The oxygen content was controlled by the p_{O_2}–t equilibrium with the gas atmosphere. Oxides were annealed in a quenching apparatus consisting of a vertical tube furnace with both top and bottom gas inlets and an outlet located just above the quenching metal flange. The equilibration at 900°C lasted 5–8 days and was longest for samples close to the stoichiometric oxygen content, $w = 0$. The rate of quenching into dry, high-purity Ar (<1 ppm O_2) corresponded to an elapse of 5 s before the red glow had disappeared.

Partial pressures of oxygen above $p_{O_2} = 10^{-4}$ bar were obtained by mixing O_2 with Ar; lower values were controlled by the high-temperature equilibrium occurring in the premixed flow of argon, hydrogen (5N purity), and water vapor. The water vapor was introduced from a ~ 45 wt% solution of H_3PO_4 at room temperature, and the saturated partial pressure of $p_{H_2O} \approx 0.02$ bar was corrected for the actual temperature and concentration of the H_3PO_4 solution. The high-temperature composition of the gas was calculated from the dilution ratios and the thermodynamic data (9, 10) for the H_2O formation.

Oxygen Content Analysis

The oxygen content of all samples was determined cerimetrically. Samples with $w < 0$ (~ 0.15 g, in the form of fine powder) were dissolved in 5 ml of water and 4 ml of concentrated HCl in a 10-ml ampoule, sealed under Ar. Samples with $w > 0$ were dissolved in 2 ml of water and 6 ml of concentrated HCl in a 10-ml ampoule, sealed under Ar together with < 0.15 g of Mohr's salt upon which the molarity of the cerimetric solution had previously been determined. For compositions close to $w = 0$, amounts were scaled up by a factor of two. Dissolution at 50–60°C was aided by ultrasound stirring and lasted ~ 5 min. The resulting solutions were complexed with 10 ml of concentrated phosphoric acid and titrated at room temperature under Ar with ferroin as an indicator.

Powder X-Ray Diffraction

The phase purity and unit-cell parameters were evaluated from powder X-ray diffraction (PXD) data obtained with a Guinier–Hägg camera with Cu$K\alpha_1$ radiation and Si as an internal standard. The photographs were scanned by an LS-18 film scanner with software for X-ray data treatment (11).

Mössbauer Spectroscopy

The spectra were recorded at room temperature in transmission geometry and fitted using the full Hamiltonian of combined electric and magnetic interactions. The Mössbauer absorbers were prepared by mixing ~ 80 mg of sample material with varnish and evenly distributing it on an iron-free aluminum foil. The absorber diameter was 19 mm. The measurements were performed with an Amersham ^{57}Co:Rh (20 mCi, January 1995) source, recorded between January and August 1997. A linear velocity scale with a maximum of 15 mm/s was applied. The following principal hyperfine parameters were obtained from the fitted spectra: the internal magnetic field experienced by the

Fe nucleus (B), the chemical isomer shift relative to α-Fe (δ), the quadrupole coupling constant (eQV_{zz}), the resonance line width (Γ), and the relative intensities of the components (I). The following conditions and constraints were applied: (i) Each component was allowed a certain variation in the parameter B to simulate the effect of local distortions of the coordination polyhedra (see ref 1). A Gaussian distribution was assumed and its width (ΔB) was introduced as a fit parameter. Components corresponding to various valence states were allowed to have different values of ΔB. When several components corresponded to the same valence state, they were constrained to have the same values of ΔB, except for the oxidized samples, in which no constraints were applied to ΔB. The resonance line width (Γ) was the same for all components. In the actual fits the maximum values for ΔB were found to vary from ~ 3 T for the most reduced samples to ~ 1 T at $w = 0$ to ~ 4 T for the most oxidized samples. (ii) According to ref 12, the internal magnetic field in $YBa_2Fe_3O_{8+w}$ is perpendicular to the c axis, whereas the main component V_{zz} of the electric field gradient (EFG) lies along c for both the five- and six-coordinated Fe(2) and Fe(1) sites. In the fitting procedure, the angle θ between V_{zz} and B was thus given an initial value of 90°. For the spectral components observed only for the reduced samples (i.e., components associated with Fe^{2+}), θ was given values close to zero. (The different situation for θ in the reduced samples originates from the fact that the vacancies associated with the formation of Fe^{2+} species are found in the a, b plane of their octahedral environment; see also Sections (IIIB and IIIC). The asymmetry parameter η of the EFG was set to zero to keep the number of refined parameters low. That this constraint is actually true for the major components in the tetragonal phase was also tested in practice. (iii) A small asymmetric quadrupole component, originating from traces of iron in the Be detector window, was kept fixed during the fit. The latter impurity defect covers less than 1% of the spectral intensity obtained in the measurements.

III. RESULTS

A. Compositional Characterizations

According to PXD, the bulk samples were of the triple-perovskite type. The products contained around 1% of cubic (Ba,*RE*) $FeO_{\sim 3}$, which usually occurs despite precautions taken to ensure the exact stoichiometry of the metals in these triple-perovskite-type phases. This admixture easily shows up since it lies in close vicinity of the main phase in the phase diagram (13). It is probable that it occurs as a consequence of a slight fractional occupation of *RE* at the Ba site rather than of incorrect proportions of the starting materials.

The controlled variations of the oxygen content showed that the $RE = Er$ variant is the least stable of the three phases with respect to both temperature and p_{O_2}. In oxidizing atmospheres (when $w > 0$), a gradual solid-state decomposition of $ErBa_2Fe_3O_{8+w}$ is seen after several days at 1100°C, whereas the Dy and Y variants melt incongruently around 1250°C. In reducing atmospheres (when $w < 0$), the melting point for all three $REBa_2Fe_3O_{8+w}$ phases decreases rapidly toward 900°C for the most reduced composition. Subjected to a decrease in p_{O_2}, the $RE = Er$ phase appears to have the lower homogeneity limit at 900°C around $w = -0.20$, whereas $w \approx -0.25$ is the limit for $RE = Dy$ and Y. The upper homogeneity limit at 900°C is not crossed at $p_{O_2} = 1$ bar.

The compositions and the quenching conditions of the samples used for the Mössbauer measurements are illustrated in Fig. 1. In accordance with the structural features, the experimental points are fitted by a simple model for point-defect equilibria in $REBa_2Fe_3O_{8+w}$, where oxygen interstitials prevail when $w > 0$:

$$O_2 \rightleftharpoons 4h^{\cdot} + 2O_i'' \qquad [1]$$

and oxygen vacancies when $w < 0$:

$$2O_O^{\times} \rightleftharpoons 4e' + 2V_O^{\cdot\cdot} + O_2 \qquad [2]$$

Since $w = [O_i''] - [V_O^{\cdot\cdot}]$, the electroneutrality condition $[e'] + 2w = [h^{\cdot}]$ combined with equilibrium-constant terms for Eqs. [1] and [2] and the (anti-)Frenkel equilibrium gives w as a function of $\log p_{O_2}$, with these three equilibrium constants as parameters. It can be seen from the fitted curves that the oxygen contents in the samples are reasonably consistent both mutually and with the model.

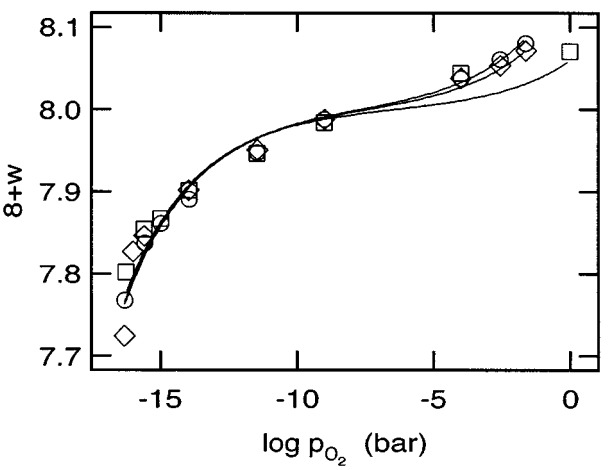

FIG. 1. Quenching conditions for $REBa_2Fe_3O_{8+w}$ at 900°C. RE = Dy (○), Er (□), and Y (◇).

In a powder state, the samples containing Fe^{2+} tend to oxidize slowly at room temperature. Despite precautions (Ar protective atmosphere), the oxygen content was found to increase by $\Delta w = 0.01$–0.02 (most for the most reduced compositions) in the period of around a month between the synthesis and the collection of the Mössbauer spectra. The oxidation proceeds also on aging of the varnish-covered Mössbauer probes, as evidenced by the fitting of spectra remeasured a few months later and the average valence states which resulted from these.

B. Structural Characterizations

Plots of the unit-cell parameters versus the oxygen content for the actual samples which were subjected to Mössbauer spectroscopy are shown in Fig. 2. The crystal structure of REBa$_2$Fe$_3$O$_{8+w}$ is tetragonal (Fig. 3) except for the most reduced compositions, where an orthorhombic distortion occurs. When $w > 0$, the site O(4) acquires a partial occupancy and the inserted oxygen atoms induce split-position defects, O(2A) and O(2B), on the neighboring oxygen atoms, as indicated in Fig. 3. Probably, also the O(1) site is affected by the added oxygen atoms. When $w < 0$, oxygen vacancies form at the O(3) site. For further details on structural aspects, see refs 2–4.

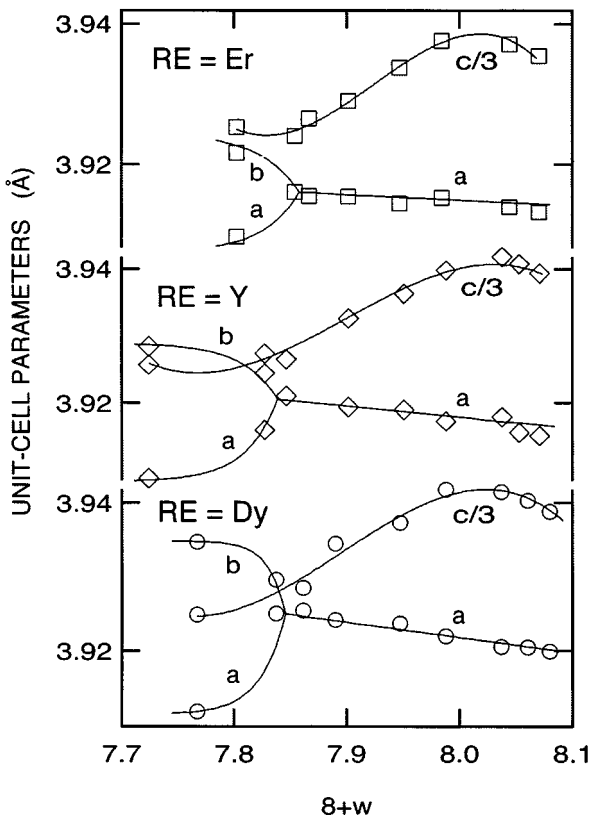

FIG. 2. Unit-cell parameters a, b, and $c/3$ versus oxygen content for the REBa$_2$Fe$_3$O$_{8+w}$ samples used for Mössbauer measurements. Calculated standard deviations do not exceed the size of the symbols.

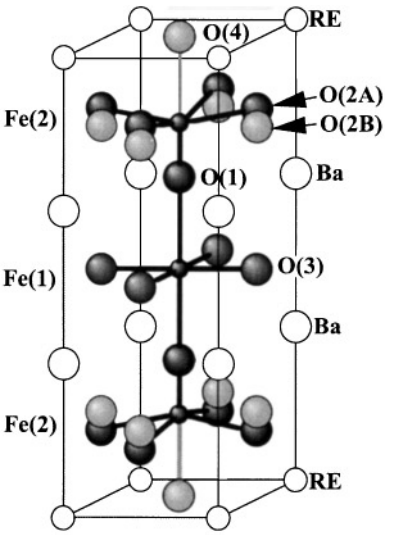

FIG. 3. Schematic representation of the crystal structure of tetragonal REBa$_2$Fe$_3$O$_{8+w}$ according to ref 3.

C. Mössbauer Spectra

Representative examples of the typical features of the Mössbauer spectra and their fitted curves are shown in Fig. 4. All spectra are typical of an AF ordering, and, altogether, five AF components have been identified. Two of them dominate in all spectra and were assigned to the trivalent iron with spin state $S = \frac{5}{2}$ in octahedral ($^{CN6}_{AF}Fe^{3+}_{S5/2}$) and square-pyramidal ($^{CN5}_{AF}Fe^{3+}_{S5/2}$) environment. The three remaining components were assigned to $^{CN5}_{AF}Fe^{2+}_{S2}$, $^{CN4}_{AF}Fe^{2+}_{S2}$, and $^{CN6}_{AF}Fe^{4+}_{S2}$. In all spectra, a paramagnetic component designated $_P$Fe is also present, with intensity increasing from $\sim 1\%$ for $w \approx 0$ to 3–4% for both the most oxidized and the most reduced samples.

Assignments of the Spectral Components

Internal fields. The internal magnetic fields B at the iron nuclei for the various Mössbauer components are shown in Fig. 5 as functions of the oxygen content parameter w for RE = Dy, Er, and Y. The high values of the internal fields for all components suggest high-spin states. The $^{CN6}_{AF}Fe^{4+}_{S2}$ component has a somewhat lower field, which still is in line with the $S = 2$ state considering the possible variations in the spin density and the orbital term.

Isomer shifts. The isomer shifts of the Mössbauer components are shown in Fig. 6 as functions of w in REBa$_2$

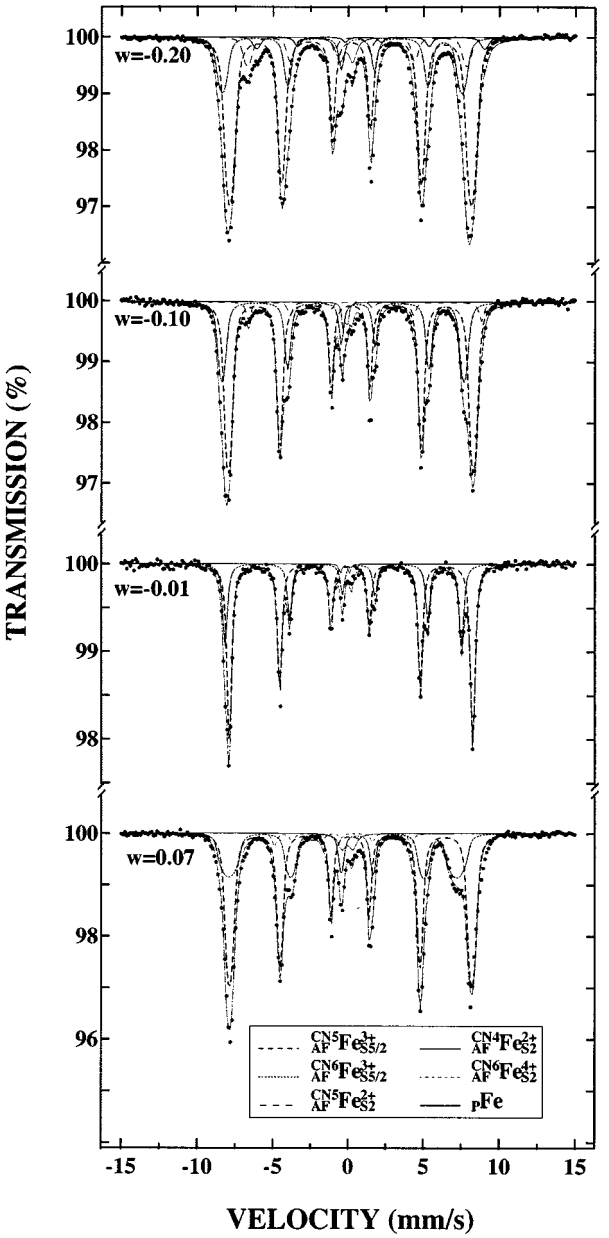

FIG. 4. Mössbauer spectra of selected $ErBa_2Fe_3O_{8+w}$ samples at 296 K. Labeling of the components is shown at the bottom of the illustration.

Fe_3O_{8+w}. The components $^{CN6}_{AF}Fe^{3+}_{S5/2}$ and $^{CN5}_{AF}Fe^{3+}_{S5/2}$ have δ close to 0.30 mm/s along the entire range of w, which fits all the spin states of trivalent iron, but none of tetravalent iron, as given in refs 5 and 14. The $_{AF}Fe^{2+}_{S2}$ components have the highest isomer shifts, and this supports both the valence state and spin assignments since low-spin divalent states would have lower δ. The $^{CN6}_{AF}Fe^{4+}_{S2}$ component has a negative δ and is the only possible candidate in its range of δ except for a low-spin trivalent iron. The latter, however, would be expected to have a lower internal field.

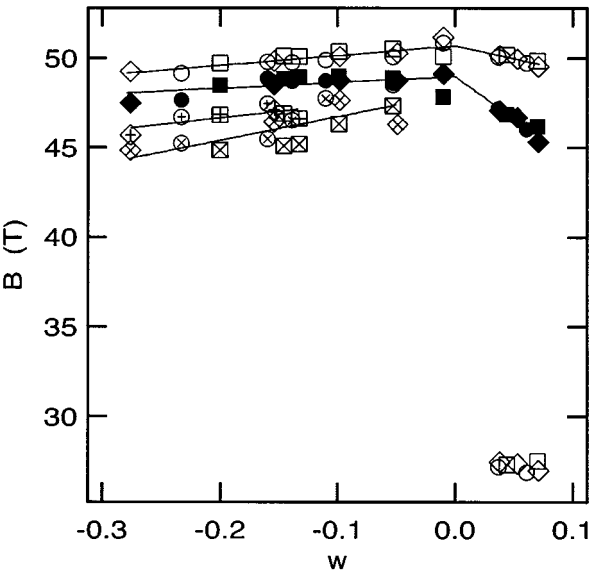

FIG. 5. Internal fields of the $REBa_2Fe_3O_{8+w}$ Mössbauer spectra. RE = Dy (○), Er (□), and Y (◇). Component symbols: $^{CN6}_{AF}Fe^{3+}_{S5/2}$, filled; $^{CN5}_{AF}Fe^{3+}_{S5/2}$, empty; $^{CN5}_{AF}Fe^{2+}_{S2}$, crossed; $^{CN4}_{AF}Fe^{2+}_{S2}$, horizontally crossed, $^{CN6}_{AF}Fe^{4+}_{S2}$, dot-centered. Standard deviations do not exceed the size of the symbols. Lines are fitted as guides for the eye.

Quadrupole coupling constants. The quadrupole coupling constants of the AF components are shown in Fig. 7 as functions of w. The largest eQV_{zz} value is obtained for $^{CN6}_{AF}Fe^{3+}_{S5/2}$. This somewhat surprising finding has its origin in the elongation of the Fe(1) coordination octahedron, where according to ref 2 the O(1)–Fe(1) distance is 2.13 Å whereas

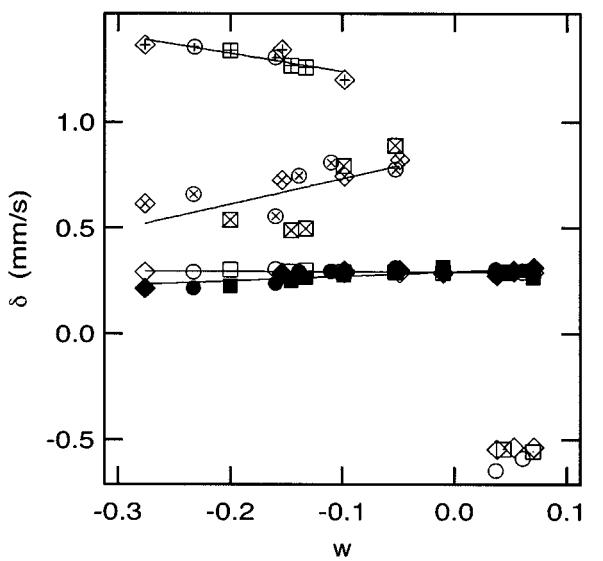

FIG. 6. Isomer shifts of the $REBa_2Fe_3O_{8+w}$ Mössbauer spectra. RE = Dy (○), Er (□), and Y (◇). Component symbols: $^{CN6}_{AF}Fe^{3+}_{S5/2}$, filled; $^{CN5}_{AF}Fe^{3+}_{S5/2}$, empty; $^{CN5}_{AF}Fe^{2+}_{S2}$, crossed; $^{CN4}_{AF}Fe^{2+}_{S2}$, horizontally crossed; $^{CN6}_{AF}Fe^{4+}_{S2}$, dot-centered. Standard deviations do not exceed the size of the symbols. Lines are fitted as guides for the eye.

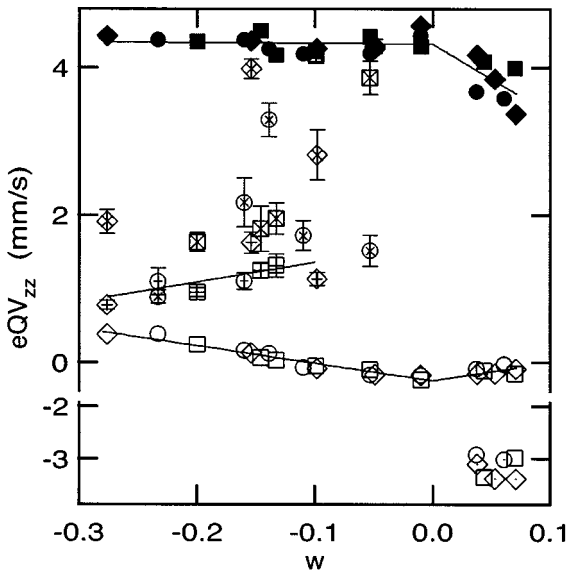

FIG. 7. Quadrupole coupling constants of the REBa$_2$Fe$_3$O$_{8+w}$ Mössbauer spectra. RE = Dy (○), Er (□), and Y (◇). Component symbols: $^{CN6}_{AF}Fe^{3+}_{S5/2}$, filled; $^{CN5}_{AF}Fe^{3+}_{S5/2}$, empty; $^{CN5}_{AF}Fe^{2+}_{S2}$, crossed; $^{CN4}_{AF}Fe^{2+}_{S2}$, horizontally crossed; $^{CN6}_{AF}Fe^{4+}_{S2}$, dot-centered. Standard deviations are shown when they exceed the size of the symbols. Lines are fitted as guides for the eye.

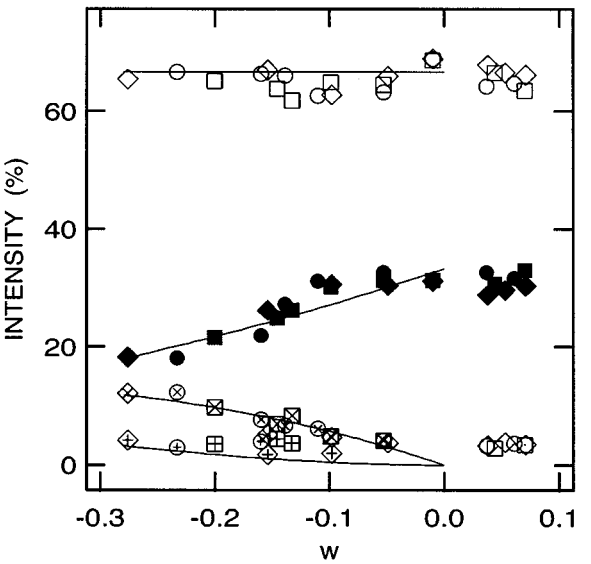

FIG. 8. Component intensities in the REBa$_2$Fe$_3$O$_{8+w}$ Mössbauer spectra. RE = Dy (○), Er (□), and Y (◇). Component symbols: $^{CN6}_{AF}Fe^{3+}_{S5/2}$, filled; $^{CN5}_{AF}Fe^{3+}_{S5/2}$, empty; $^{CN5}_{AF}Fe^{2+}_{S2}$, crossed; $^{CN4}_{AF}Fe^{2+}_{S2}$, horizontally crossed; $^{CN6}_{AF}Fe^{4+}_{S2}$, dot-centered. Standard deviations do not exceed the size of the symbols. Curves represent the proportions of individual CN of the total Fe in the reduced region; Fe(1): CN6, CN5, and CN4 by statistical distribution according to Eq. [3], Fe(2): CN5 constant.

O(3)–Fe(1) is only 1.96 Å. Since the spherically symmetrical half-full valence shell of high-spin Fe^{3+} does not contribute to eQV_{zz}, the coupling constant reflects mainly the symmetry of the ligands. For the same reason, the quadrupole coupling constant is nearly zero for $^{CN5}_{AF}Fe^{3+}_{S5/2}$, viz., the square-pyramidal oxygen coordination where the Fe(2) atom is situated practically in the center of the coordination polyhedron (2–4). In the square-pyramidal as well as the octahedral situation, V_{zz} is parallel with the c axis, viz., $\theta = 90°$. If the Fe(1) octahedron were flattened and not elongated, eQV_{zz} would be large and negative. Such a geometry is obtained for the Fe(2) coordination when the added oxygens are inserted at the O(4) site (see Fig. 3). The negative eQV_{zz} for $^{CN6}_{AF}Fe^{4+}_{S2}$ with V_{zz} oriented along the c axis ($\theta = 90°$) pins this component unambiguously in the structural environment. The small changes seen in these eQV_{zz} values as a function of w must be attributed to the structural deformations caused by the change in the oxygen content. The quadrupole coupling constants for $^{CN4}_{AF}Fe^{2+}_{S2}$ and $^{CN5}_{AF}Fe^{2+}_{S2}$ are relatively large (and positive), and this shows that they also originate from the initially octahedral lattice site. Both are found to be perpendicular to the c axis ($\theta = 0°$), in line with the orientations of the coordination polyhedra emerging through the vacancy formation at the O(3) site. The wide scatter in eQV_{zz} for $^{CN4}_{AF}Fe^{2+}_{S2}$ and $^{CN5}_{AF}Fe^{2+}_{S2}$ as functions of w is apparently associated with variations in coordination geometries upon the formation of vacancies. In addition, it should be remembered that both components have low intensities.

Intensities. The observed intensities of the AF components are shown in Fig. 8 as a function of the oxygen content parameter w (the intensity of the weak and poorly resolved paramagnetic component is neglected). The intensity distribution in Fig. 8 immediately leads to the assignment of $^{CN6}_{AF}Fe^{3+}_{S5/2}$ (32% relative intensity for $w = 0.00$) to the Fe(1) site and $^{CN5}_{AF}Fe^{3+}_{S5/2}$ (68% relative intensity for $w = 0.00$) to the Fe(2) site. As the latter is almost constant throughout the range of w and the former decreases with decreasing w for $w < 0$, the site assignments are ascertained. The assignments of $^{CN5}_{AF}Fe^{4+}_{S2}$, $^{CN5}_{AF}Fe^{2+}_{S2}$, and $^{CN4}_{AF}Fe^{2+}_{S2}$, as shown in Fig. 8, are in conformity with their expected variations with the oxygen content parameter w. A further check on the component assignments by their intensities can be obtained from the intensity-weighted summation of the assigned valence states. Figure 9 shows that a good agreement is obtained with the chemically determined oxidation state of iron.

IV. DISCUSSION

A consistent assignment of the spectral components observed in the REBa$_2$Fe$_3$O$_{8+w}$ phases emerged from the overall behavior of the experimental hyperfine parameters. In particular, we have unequivocally shown that both the Fe(1) and Fe(2) lattice sites are populated by high-spin Fe^{3+}, which disagrees with the findings of Yuen *et al.* (15) for the $Y_{1-x}Pr_xBa_2Fe_3O_8$ phase. The only charge imbalance

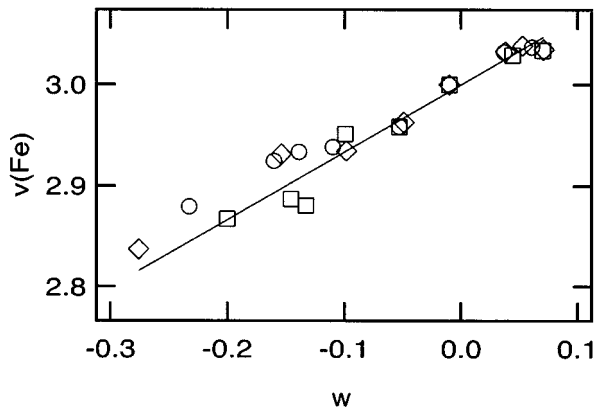

FIG. 9. Average valence of Fe, based on the statistics of the Mössbauer components, versus oxygen content parameter w. Standard deviations do not exceed the size of the symbols. Line shows the dependence according to $RE\mathrm{Ba_2Fe_3O_{8+w}}$. RE = Dy (○), Er (□), and Y (◇).

in $RE\mathrm{Ba_2Fe_3O_{8+w}}$ arises from distribution of Fe^{2+} at the Fe(1) site and Fe^{4+} at the Fe(2) site as the oxygen content is varied. (Owing to the high Néel temperature, $T_N \approx 650$ K (3, 4), and the predominant Fe^{3+} in $RE\mathrm{Ba_2Fe_3O_{8+w}}$, our magnetic susceptibility measurements were not suited to corroborate the presence of Fe^{2+} and Fe^{4+}.)

In general, all Mössbauer components found in the ordered $RE\mathrm{Ba_2Fe_3O_{8+w}}$ triple-perovskite-type phases have their counterparts in the cubic disordered $\mathrm{LaBa_2Fe_3O_{8+w}}$ (1). As the homogeneity region for the latter extends into highly oxidized states ($w \to 1$), the assignments of components related to tetravalent Fe are less ambiguous than in the present case, where, on the other hand, much better resolution is achieved in the reduced region ($w < 0$). For hyperfine parameters that can be structurally averaged, there is a close correspondence between the two structure variants. As an example, at $w = 0$ the average magnetic field is 49.3 T in the triple-perovskite-type phases, whereas the corresponding value for the disordered cubic (La) variant is 47.9 T (1).

However, there is a large difference between the 27-T field obtained for Fe^{2+}_{S2} in the RE = La phase and the 48-T field seen in the present phases. This is understood by the fact that the internal field at the Fe^{2+}_{S2} nucleus is composed of mainly two contributions: a spin term and an orbital term (16). In the cubic phase, we imagine that these terms add destructively, whereas for the triple-perovskite-type phase they add constructively. From the values 28 and 48 T, a rough estimate for the orbital term gives $(48 - 28)/2 = 10$ T (neglecting other terms). Thus the spin-only contribution to the internal field at Fe^{2+}_{S2} for RE = La as well as Dy, Er, and Y would be some 38 T. This relates well to the 50-T field at the $Fe^{3+}_{S5/2}$ nuclei since the ratio of the spins (2/(5/2)) matches the ratio of the fields (~ 0.8). Note that also the 28-T field of the Fe^{4+}_{S2} component fits this picture, as both its spin and angular momentum are equal to those of Fe^{2+}_{S2}.

The structural difference between the disordered and ordered $RE\mathrm{Ba_2Fe_3O_{8+w}}$ variants is clearly reflected in the Mössbauer spectra. Whereas a random binomial distribution of oxygen vacancies applies for the iron states in the disordered variant (1), the trivalent Fe states in the ordered, triple-perovskite-type variant are clearly in the ratio of the two structural coordination polyhedra. Hence the nearly equal proportion of the CN6 : CN5 states for RE = La at $w = 0$ is changed to 1 : 2 for the triple-perovskite type of the same composition. As long as the triple-perovskite-type structure is present, the iron valence and spin state parameters are affected little by the variations between RE = Dy, Er, and Y.

The essential structural information to be extracted from the Mössbauer experiments is the information on the occurring disorder rather than order, as the latter is available from diffraction methods. There are three kinds of disorder in the triple-perovskite-type structure: (i) disorder of the extra oxygen atoms around the Fe(2) site when $w > 0$, (ii) disorder of the oxygen vacancies around the Fe(1) site when $w < 0$, and (iii) the possible (anti-)Frenkel-type disorder of both these defects. The intensities of the Mössbauer components carry information about the statistics of all relevant individual coordination states, but, as discussed earlier, well-resolved quantitative information was obtained only in the $w < 0$ region.

To evaluate this disorder, intensities of ${}^{\mathrm{CN5}}_{\mathrm{AF}}\mathrm{Fe}^{2+}_{S2}$ and ${}^{\mathrm{CN4}}_{\mathrm{AF}}\mathrm{Fe}^{2+}_{S2}$ at the Fe(1) site are tested according to a model with a binomial distribution of vacancies situated at the O(3) site. In terms of w, the probabilities (p) for having 4, 3, and 2 O(3) atoms around a given Fe(1) are

$$p(\mathrm{CN6}) = \left(\frac{2+w}{2}\right)^4,$$

$$p(\mathrm{CN5}) = \left(\frac{2+w}{2}\right)^3 \left|\frac{w}{2}\right| \binom{4}{1},$$

$$p(\mathrm{CN4}) = \left(\frac{2+w}{2}\right)^2 \left|\frac{w}{2}\right|^2 \binom{4}{2}. \qquad [3]$$

Taking into account that Fe(1) represents 1/3 of the iron atoms and neglecting coordination numbers less than 4, the predictions for intensities of the ${}^{\mathrm{CN6}}_{\mathrm{AF}}\mathrm{Fe}^{3+}_{S5/2}$, ${}^{\mathrm{CN5}}_{\mathrm{AF}}\mathrm{Fe}^{2+}_{S2}$, and ${}^{\mathrm{CN4}}_{\mathrm{AF}}\mathrm{Fe}^{2+}_{S2}$ components are displayed in Fig. 8.

Another structural feature which was expected to be reflected in the hyperfine Mössbauer parameters was the change in the symmetry from tetragonal to orthorhombic for low values of w. The only parameter which conveys some indication on this symmetry conversion is eQV_{zz} in Fig. 7. On careful examination of the data points for ${}^{\mathrm{CN5}}_{\mathrm{AF}}\mathrm{Fe}^{2+}_{S2}$, a peak around $w = -0.15$ may be imagined for all three RE elements. This probably could reflect the conversion, in which case, the absence of such a peak for the other

components can be explained by assuming the tetragonal to orthorhombic conversion to deform the oxygen coordinations (to a first-order approximation) in the following manner: oxygen atoms with coordinates $x = y = \pm a/2$ in the tetragonal case will be $x = \pm(a/2 - \Delta)$ and $y = \pm(a/2 + \Delta)$ in the orthorhombic case. (When elaborated in detail, the use of point charges for the various oxygen environments and lattice summation over nearest oxygen neighbors would have to be performed; cf. ref 16.) This very simple model then leaves the six- and five-coordinated trivalent Fe atom with no change in eQV_{zz} as opposed to the nonzero value for the divalent Fe atoms. Neglecting valence–electron contributions to eQV_{zz}, the $^{CN5}_{AF}Fe^{2+}_{S2}$ component should be affected twice as much as the $^{CN4}_{AF}Fe^{2+}_{S2}$ term. In other words, mainly η would be changed, unless V_{zz} is perpendicular to the c axis.

The eQV_{zz} parameter obtained when fitting the spectra can be elaborated further. In particular, the substantial value obtained for the $^{CN4}_{AF}Fe^{2+}_{S2}$ component indicates that the four-coordinated oxygen environment indeed is planar and not tetrahedral. In the actual fit, the θ angle was not fixed; nevertheless a zero was obtained within the fitting error. Only for the $^{CN5}_{AF}Fe^{2+}_{S2}$ component θ constantly approached 36°, indicating a slight deformation of the "rhombo-planar" pyramidal oxygen neighborhood or compensating for the neglect of the η parameter.

ACKNOWLEDGMENTS

All Mössbauer measurements were performed by J.M. at the Helsinki University of Technology with the kind permission of T. Katila, head of the Mössbauer research group.

REFERENCES

1. J. Lindén, M. Lippmaa, P. Karen, A. Kjekshus, and M. Karppinen, *J. Solid State Chem.* **138,** 87 (1998).
2. Q. Huang, P. Karen, V. L. Karen, A. Kjekshus, J. W. Lynn, A. D. Mighell, N. Rosov, and A. Santoro, *Phys. Rev. B*: *Condens. Matter* **45,** 9611 (1992).
3. P. Karen, A. Kjekshus, Q. Huang, J. W. Lynn, N. Rosov, I. Natali-Sora, V. L. Karen, A. D. Mighell, and A. Santoro, *J. Solid State Chem.* **136,** 21 (1998).
4. Q. Huang, P. Karen, V. L. Karen, A. Kjekshus, J. W. Lynn, A. D. Mighell, N. Rosov, and A. Santoro, to be published.
5 T. C. Gibb and M. Matsuo, *J. Solid State Chem.* **81,** 83 (1989).
6. J. M. Gonzáles-Calbet, M. Parras, M. Vallet-Regí, and J. C. Grenier, *J. Solid State Chem.* **92,** 110 (1991).
7. E. García-González, M. Parras, J. M. González-Calbet, and M. Vallet-Regí, *J. Solid State Chem.* **104,** 232 (1993).
8. P. Karen and A. Kjekshus, *J. Am. Ceram. Soc.* **77,** 547 (1994).
9. I. Barin and O. Knacke, "Thermochemical Properties of Inorganic Substances," pp. 316, 584. Springer, Berlin, 1973.
10. I. Barin, O. Knacke, and O. Kubashevski, "Thermochemical Properties of Inorganic Substances, Supplement," p. 295. Springer, Berlin, 1977.
11. P. E. Werner, The Computer Programme SCANPI 9, Institute of Inorganic Chemistry, University of Stockholm, Stockholm, Sweden, 1992.
12. I. Felner, I. Nowik, U. Yaron, O. Cohen, E. R. Bauminger, T. Kroener, and G. Czjzek, *Phys. Rev. B*: *Condens. Matter* **48,** 16040 (1993).
13. P. Karen, P. H. Andresen, and A. Kjekshus, *J. Solid State Chem.* **101,** 48 (1992).
14. N. N. Greenwood and T. C. Gibb, "Mössbauer Spectroscopy" p. 91. Chapman and Hall, London, 1971.
15. T. Yuen, M. Seyedahmadian, R. E. Salomon, G. H. Myer, and G. Cao, *J. Appl. Phys.* **79,** 6001 (1996).
16. P. Gütlich, *in* "Mössbauer Spectroscopy" (U. Gonser, Ed.), p. 82. Springer, Berlin, 1975.